AIP | Journal of Applied Physics

Time-resolved optical emission spectroscopy of laser-produced air plasma

J. J. Camacho, L. Díaz, M. Santos, L. J. Juan, and J. M. L. Poyato

Citation: J. Appl. Phys. **107**, 083306 (2010); doi: 10.1063/1.3382914
View online: http://dx.doi.org/10.1063/1.3382914
View Table of Contents: http://jap.aip.org/resource/1/JAPIAU/v107/i8
Published by the American Institute of Physics.

Time-resolved optical emission spectroscopy of laser-produced air plasma

J. J. Camacho,[1,a)] L. Díaz,[2] M. Santos,[2] L. J. Juan,[1] and J. M. L. Poyato[1]
[1]*Departamento de Química-Física Aplicada, Facultad de Ciencias, Universidad Autónoma de Madrid, Cantoblanco, 28049 Madrid, Spain*
[2]*Instituto de Estructura de la Materia, CFMAC, CSIC, Serrano 121, 28006 Madrid, Spain*

(Received 27 October 2009; accepted 9 March 2010; published online 26 April 2010)

Time-resolved optical emission spectroscopy (OES) is used to analyze a mesh-initiated air breakdown plasma induced by a transverse excitation atmospheric CO_2 pulsed laser ($\lambda = 10.591$ μm, 64 ns (full width at half maximum), 70–160 J/cm^2). Emission from excited N, O, C, H, and Ar; ionic fragment N^+, O^+, N^{2+}, O^{2+}, C^+, and molecular band systems of $N_2^+(B\ ^2\Sigma_u^+ - X\ ^2\Sigma_g^+$; $D\ ^2\Pi_g - A\ ^2\Pi_u)$, $N_2(C\ ^3\Pi_u - B\ ^3\Pi_g)$, and $OH(A\ ^2\Sigma^+ - X\ ^2\Pi)$ is observed. Plasma characteristics are examined in detail on the emission lines of N^+, O^+, and C by time-resolved OES technique. The results show a faster decay of continuum and ionic spectral species than of neutral atomic and molecular ones. The velocity and kinetic energy distributions for the different species were obtained from time-of-flight measurements. Excitation temperature and electron density in the laser-induced plasma were estimated from the analysis of spectral data at various times from the laser pulse incidence. Temporal evolution of electron density has been used for the estimation of the three-body recombination rate constant. © *2010 American Institute of Physics*.
[doi:10.1063/1.3382914]

I. INTRODUCTION

The absorption of light and heating of a gas is of primary significance for important practical problems (the fire ball of an explosion, the heating of artificial satellites during reentry into the atmosphere, detection of environmental pollutants, ignition systems, laser machining, inertially confined fusion, etc.). Gases such as air under normal absorption conditions are relatively transparent to laser radiation. However, if the radiant energy in the focus exceeds the threshold value for the breakdown, as happens with high-power lasers (ruby, Nd:YAG, CO_2, excimer, etc.), the gas becomes highly ionized and the plasma thus produced will practically absorb the beam. The formation of laser-induced breakdown (LIB) plasma in a gas has been investigated since its discovery[1] resulting in several studies that have been summarized by different authors.[2–14] The LIB plasma develops a shock wave into the ambient medium and the gas is heated to high temperatures (1–3 eV).[15] After breakdown, the plasma becomes very opaque and an abrupt shutoff of the laser transmitted light occurs. Due to the many experimental parameters involved in the LIB, an exhaustive investigation of the plasma would involve the processing of an impressive number of records. Because of the transient features of the plasma created by LIB, optical emission spectroscopy (OES) technique with time and space resolution is especially appropriate to obtain information about the behavior of the created species in space and time as well as the dynamics of the plasma evolution.

The LIB technique, using Nd:YAG laser, in air with temporal resolution has been used by several researchers.[16–20] The wavelength measurements of emission spectra of the CO_2 LIB plasma in N_2, O_2, and air have been reported recently by us.[21–23] We have also reported studies on the temporal evolution of the LIB plasma of graphite.[24] Time-resolved OES studies of mesh-initiated air breakdown induced by a high-power transverse excitation atmospheric (TEA) CO_2 pulsed laser, have not been reported before.

The present paper is aimed at discussing temporal plasma processes produced by high-power IR CO_2 pulsed laser on ambient air and at evaluating plasma emission changes which are of fundamental importance in establishing the mechanisms responsible for the plasma emission. We present some results obtained from the time-resolved spectroscopic analysis of the LIB air plasma. We discuss the dynamics of the plasma expansion and formation of different atomic, ionic, and molecular species for different delay times with respect to the beginning of the laser pulse. The velocity and kinetic distributions for the different species were obtained from the time-of-flight (TOF) measurements using time-resolved OES.[25,26] Possible mechanisms for the production of these distributions are discussed. Line intensities from N^+ were used for determining electron temperature. Stark-broadened profiles were employed to calculate electron density. The temporal behavior of electron number density has been used for the estimation of three-body recombination rate constant and recombination time.

II. EXPERIMENTAL SETUP

The experimental setup is shown in Fig. 1. The experiments were carried out with TEA CO_2 laser (Lumonics model K-103) operating on an 8:8:84 mixture of CO_2:N_2:He, respectively, at a wavelength of 10.591 μm. A beam splitter was used to redirect 10% of the laser pulse energy on a pyroelectric detector (Lumonics 20D) or on a photon-drag detector (Rofin Sinar 7415) through a digital oscilloscope (Tektronix TDS 540) for energy and temporal

a)FAX: +34914974512. Electronic mail: j.j.camacho@uam.es.

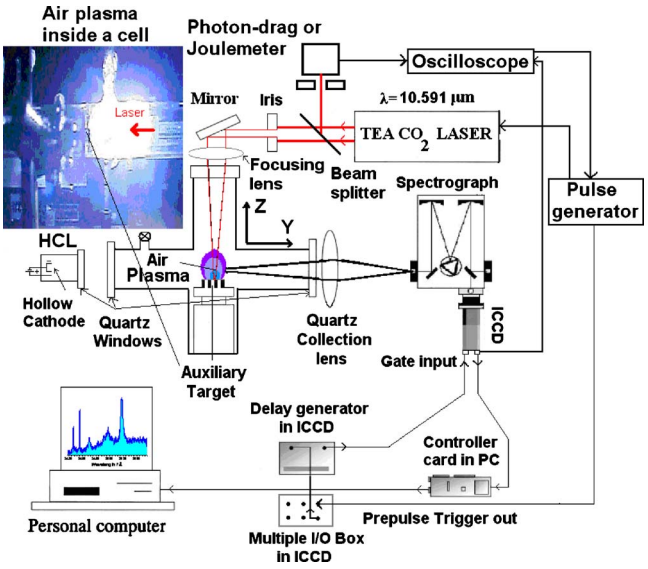

FIG. 1. (Color online) Schematic diagram of the experimental setup of time gated ICCD for pulsed laser air breakdown diagnostics. A photograph of the TEA CO_2 laser plasma (71 J/cm^2) inside a cell is included.

shape monitoring and triggering, respectively. The shot-to-shot fluctuation of the laser energy was approximately 5%. The temporal shape of the TEA CO_2 laser pulse consisted in a prominent spike of a full width at half maximum (FWHM) ≈64 ns followed by a long lasting tail of lower energy and about 3 μs duration (see Fig. 2). The primary laser beam was angularly defined and attenuated by a diaphragm of 17.5 mm diameter just before the focusing lens. The measured maximum laser energy was 3160 mJ, leading to an estimated power of 49.5 MW, intensity (power density or irradiance) of 6.31 GW cm^{-2}, fluence of 402 J cm^{-2}, photon flux of 3.4×10^{29} photon cm^{-2} s^{-1}, and electric field of 1.63 MV cm^{-1} on the target surface. The laser pulse fluence

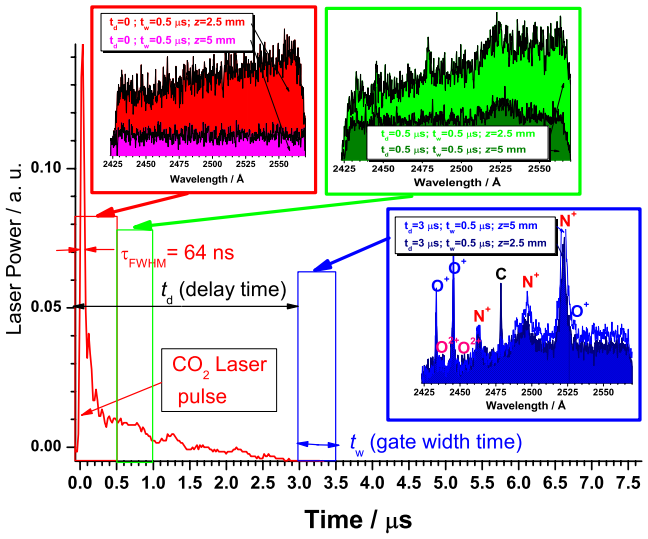

FIG. 2. (Color online) A schematic overview of the temporal history of LIB air plasma. Here t_d is the delay time and t_w is the gate width time during which the plasma emission is monitored. Inset plots illustrate some spectra observed at different delay times (0, 0.5, and 3 μs) for a fixed gate width time of 0.5 μs and z=2.5 and 5 mm. The temporal shape of the CO_2 laser pulse is also shown.

was varied in the interval 70–160 J/cm^2 with the aid of several calibrated CaF_2 attenuating plates. The pulsed laser light from the TEA CO_2 laser was focused by a NaCl lens of 24 cm focal lens onto the surface of a metal mesh (stainless steel and dimension of the mesh unit of 0.7×0.7 mm^2) in ambient air at atmospheric pressure. Focusing the laser on this mesh, allow us to fix the temporal and spatial origin. Although the metal mesh itself can be ablated, in our experimental conditions, mainly time- and space-resolved emission spectra from the air plasma were recorded. The focused-spot area (7.85×10^{-3} cm^2) of the laser beam was measured at the target position with a pyroelectric array detector (Delta Development Mark IV). The light emitted from the laser-induced plasma was optically imaged 1:1, at right angles to the normal of the metal mesh surface, by a quartz lens (focal length 4 cm, f-number=f/2.3) onto the entrance slit of a spectrometer (0.32 m ISA Jobin Yvon Spex HR320 with adjustable slit and holographic grating of 2400 grooves mm^{-1} at a resolution of ≈0.10 Å in first-order). The distance between the plasma axis and entrance slit was y=16 cm. Optical emission accompanying the laser-induced air plasma plume was viewed along the Y axis (i.e., parallel to the surface of the metal mesh), as a function of z (Fig. 1). The spectra were recorded by a gateable intensified charge-coupled device (ICCD) (Andor iStar DH-734, with a 1024 $\times$1024 matrix of 13×13 μm^2 individual pixels and thermoelectric cooling working at −20 °C). The spectral window for each experiment with this detection system (spectrometer+ICCD) was about 150 Å. The dark current of the ICCD was automatically subtracted from the measured spectral data for each measurement. For synchronization, the CO_2 laser was operated at the internal trigger mode and ICCD detector was operated in external and gate modes. The total insertion delay or propagation delay is the total time taken for the external trigger pulse to travel through the digital delay generator and gate the ICCD. This insertion delay time was 45±2 ns. The time jitter between the laser and the fast ICCD detector gate was about ±2 ns. The delay time t_d is the time interval between the arrival of the laser pulse on the metal mesh and the activation of the ICCD detector. The gate width time t_w is the time interval during which the plasma emission is monitored by the ICCD. Both parameters were adjusted by the digital delay generator of the ICCD detector. The resolution of the pulse delay time and the gate pulse width time was 25 ps. The CO_2 laser pulse picked up with the photon-drag detector triggered a pulse generator (Stanford DG 535) through the scope and this pulse was used as an external trigger in the ICCD camera. The laser pulse and the gate monitor output were displayed in the digital oscilloscope. In this way, by using the output of the photon-drag detector, the oscilloscope, the delay pulse generator and the gate monitor output of the ICCD camera, the gate width time t_w and the delay time t_d could be adjusted without insertion time. Several (Cu/Ne, Fe/Ne, and Cr/Ar) hollow cathode lamps were used for the spectral wavelength calibration of the spectrometers.

III. RESULTS AND DISCUSSION

When a high-power CO_2 laser pulse is focused onto a metal mesh surface, inside an air cell at the atmospheric pressure or in open-air, the intensity in the focal spot produces a rapid local heating followed by air breakdown and plasma formation. One example of LIB air plasma inside a cell is shown in Fig. 1. The onset of LIB in the air is a sudden dramatic event involving the production of more than 10^{16} electron-ion pairs and the emission of radiation characteristic of the air plasma. The structure of the LIB plasma is complex, and indeed there may be several isolated plasma regions with near ellipsoidal shape, produced along the laser beam axis[5] and observable by the naked eye. These multiple collinear plasmas in the air or in other gases at around atmospheric pressures difficult the definition of the focal region and temporal origin. These lead to inadequate or inaccurate knowledge of the spatial-temporal characteristic of the plasma intensity. On the other hand, it is well known that a gas plasma, due to the gas breakdown process, is produced when a TEA CO_2 laser is focused onto a metal sample at a gas pressure of around 1 atm, in which case practically all the laser irradiance is absorbed in the gas plasma.[27,28] It is expected that, in some medium range pressures between 0.01 torr and 1 atm, both gas and target plasmas are produced. In such a case, some interaction inevitable takes place between the gas and the target laser-induced plasmas. The plasma is a mixture of electrons, atoms, molecules, and ions, and mass from both the ablated target and the ambient gas. The interaction between the ejected mass and the surrounding air slows the expansion of the plasma. If a metal mesh is used as a target, a low amount of ablated material (difficult of quantify) will be formed but the spatial origin of the gas breakdown process will be accurately defined. After its formation near the metal mesh surface, the air breakdown plasma propagates perpendicularly to the surface at a supersonic speed. The shock wave heats up the surrounding air which is instantaneously transformed in strongly ionized plasma. The hot plasma expands and interacts with the ambient air, mainly by two mechanisms: (i) the expansion of high pressure plasma compresses the surrounding air and drives a shock wave and (ii) during this expansion, energy is transferred to the ambient air by the combination of thermal conduction, radiative transfer, and heating by the shock wave. The high temperatures and pressures produced by plasma absorption lead to thermal expansion of the plasma at high velocities, producing an audible acoustic signature, shock waves, and cavitation effects. The plasma also tends to expand back along the beam path toward the laser, a phenomenon known as "moving breakdown." A portion of the laser pulse energy is absorbed by the expanding plasma generating different types of waves.[29]

A relevant phenomenon occurring during plasma expansion is related to its capacity of absorbing the remainder of the laser pulse energy and screening the target surface. The phenomenon is called plasma shielding and its immediate effect is to reduce or stop the ablation after plasma induction.[30,31] The main process leading to plasma shielding is absorption of the laser energy by the electrons (inverse bremsstrahlung) and multiphoton ionization (mainly for shorter laser wavelengths). Due to the long temporal tail of the CO_2 laser pulse some significant fraction of its energy could heat to very high temperatures and pressures the just formed air plasma and dissociate the surrounding gas. By using a metal mesh, the plasma shielding is a desirable phenomenon since it decreases the ablated mass from the target.

A. Time-resolved emission spectra for laser-induced air plasma

Each laser shoot produces a single LIB spectrum. Two different types of spectra were recorded: time-integrated (delay time $t_d=0$ μs and gate width time $t_w \gg 30$ μs) and time-resolved. In the acquisition of time-integrated spectra, a good signal-to-noise ratio has been obtained averaging each spectrum over several successive laser pulses. Typically, the signals from 20 laser pulses are averaged and integrated over the entire emission time. For time-resolved measurements, the delay t_d and width t_w times were varied. It was verified that the plasma emission was reproducible over more than seven events by recording the same spectrum several times. The temporal history of the LIB air plasma is illustrated schematically in Fig. 2. The time for the beginning of the CO_2 laser pulse is considered as the origin of the time scale ($t=0$ μs). The insert pictures illustrate some emission spectra recorded at different delay and width times at two observation distances. The temporal shape of the CO_2 laser pulse is also shown.

Initially, the spectra have been obtained in the region 2423–2573 Å, at a delay time ranging from 0 to 30 μs at 0.5 μs intervals and at an observation distance z ranging from 1 to 10 mm. The spectral range was chosen in order to detect both, single and double ionized oxygen species and several single ionized nitrogen and atomic carbon lines. Figure 3 illustrates the time-resolved evolution from laser-induced (106 J/cm^2) air plasma monitored at 0, 0.1, 0.7, 2, 3, 4, and 5 μs gate delays for a fixed gate width time of 0.5 μs and $z=2.5$ mm. As seen in Fig. 3, during the initial stages after the laser pulse ($t_d \leq 0.7$ μs), continuum emission dominates the spectrum. Continuum radiation is due to result of free-free and free-bound transitions. As time evolves (0.7 μs$\leq t_d \leq 3.5$ μs), N^+, O^+, and O^{2+} emissions dominate the spectrum. These ionic lines quickly decrease for higher delay times, being detected up to ≈ 4.5 μs. The emission lines become progressively and spectrally narrower as a consequence of the electron number density variation. This indicates that the electron density and excitation temperature decrease during the plasma expansion. For $t_d > 3.5$ μs, C atomic emission line dominates the spectrum. This atomic line decreases for higher delay times, being detected up to ≈ 30 μs. The maximum intensity of continuum and spectral lines is reached after a characteristic time, depending on the observation distance z. By analyzing different spectra in this region, we see that C atoms are produced both in the ablated target and in the air breakdown. When the spectra were recorded near the target surface ($z < 2.5$ mm), the main con-

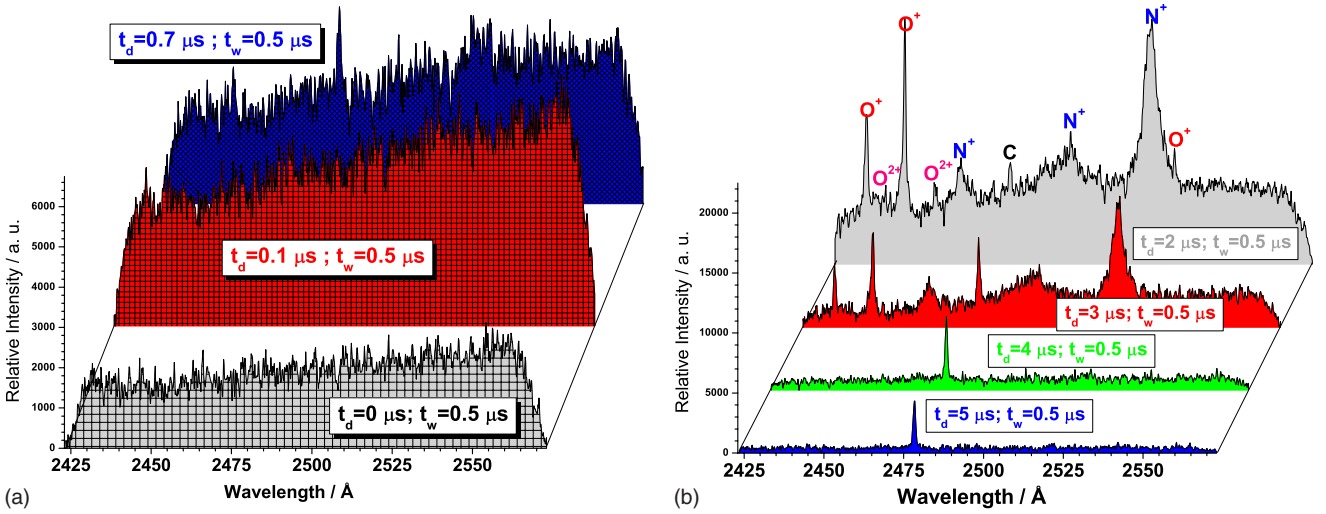

FIG. 3. (Color online) Time-resolved emission spectra from laser-induced (106 J/cm^2) air plasma observed in the region 2423–2573 Å monitored at 0, 0.1, 0.7, 2, 3, 4, and 5 μs gate delays for a fixed gate width time of 0.5 μs and z=2.5 mm.

tribution of C atoms is due to the target surface. For z >2.5 mm, practically the whole spectrum is due to air breakdown.

Figure 4 shows the time-resolved emission spectra from laser-induced air plasma (106 J/cm^2) recorded at t_d=3 μs with t_w=0.5 μs monitored at 1, 2.5, 5, 7.5, and 10 mm. In these recording conditions, the most intense plasma is monitored at 5 mm from the mesh target surface.

Figure 5 shows the temporal evolution of the LIB air plasma (71 J/cm^2) in the spectral region 3830–3960 Å, monitored at 2, 3, and 4 μs gate delays for a fixed gate width time of 0.5 μs (z=1 cm) and time-integrated spectrum (t_d=0 μs and $t_w \gg 30$ μs). The plot shows the assignment of some ionic lines of N^+, O^+, and N^{2+} and band heads of different molecular bands of $N_2^+(B\ ^2\Sigma_u^+ - X\ ^2\Sigma_g^+$; $\Delta v=0$ sequence). At early times ($t_d<1$ μs) (not shown), the plasma emission consists in a continuum. As the delay increases, some ionic lines of N^+, O^+, and N^{2+} and band heads of the molecular bands of $N_2^+(B\ ^2\Sigma_u^+ - X\ ^2\Sigma_g^+)$ enhanced as a consequence of the air plasma expansion. At longer times ($t_d>3$ μs), the ion lines significantly decrease steeply in intensity. At $t_d>5$ μs, N^+, N^{2+}, and O^+ ionic lines and N_2^+ rovibrational lines disappear.

B. TOF, velocity, and kinetic energy

Space- and time-resolved OES measurements can be used to estimate the plasma expansion rate and kinetic energy. The temporal evolution of spectral atomic, ionic, and molecular line intensities at a constant distance from the target can be used to construct the TOF profile. TOF studies of the emission provide fundamental information regarding the time taken for a particular species to evolve after the laser-induced plasma has been formed. Specifically, this technique gives an indication of the velocity of the emitted species. A rough estimation of the velocity for the different species in the plasma can be inferred from the time-resolved spectra by plotting the intensities of selected emission lines versus the

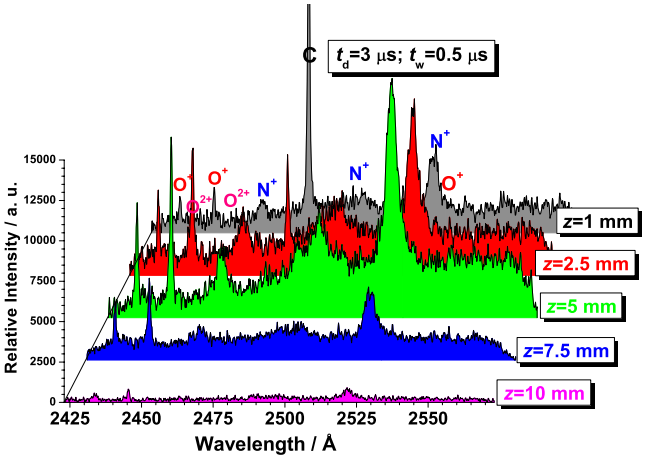

FIG. 4. (Color online) Time-resolved emission spectra from laser-induced air plasma (106 J/cm^2) observed in the region 2423–2573 Å at t_d=3 μs for t_w=0.5 μs, monitored at 1, 2.5, 5, 7.5, and 10 mm along the plasma expansion direction.

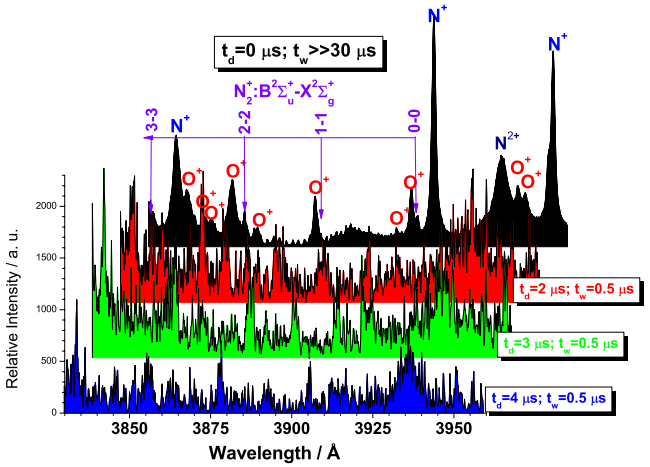

FIG. 5. (Color online) Time-resolved emission spectra from laser-induced air plasma (71 J/cm^2) observed in the region 3830–3960 Å, monitored at 2, 3, and 4 μs gate delays, for a fixed gate width time of 0.5 μs (z=1 cm) and time-integrated spectrum (t_d=0 μs and $t_w \gg 30$ μs). The assignments of some ionic lines of N^+, O^+, and N^{2+} and band heads of the molecular bands of $N_2^+(B\ ^2\Sigma_u^+ - X\ ^2\Sigma_g^+)$ are indicated.

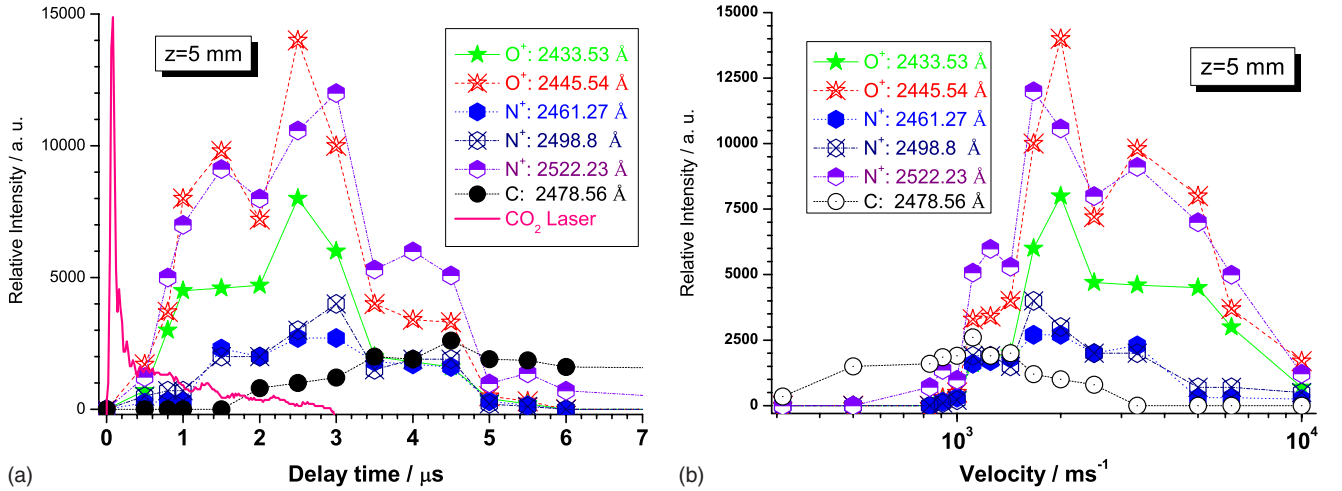

FIG. 6. (Color online) (a) Number density TOF distributions of O^+(2433.53;2445.54 Å), N^+(2461.27;2498.80;2522.23 Å), and C(2478.56 Å) lines, as a function of delay time (fixed gate width time of 0.5 μs), for a laser fluence of 106 J/cm^2 and z=5 mm. The temporal shape of the TEA CO_2 laser pulse is also shown, (b) Velocity distributions derived from the experimental TOF profiles for the indicated species.

delay time, and then calculating the velocity by dividing the distance from the target by the time where the emission peaks. This method for the determination of plasma velocity should be used with care due to the superposition of both expansion and forward movements of the plasma plume. We have assumed a plasma model consisting in two plasmas:[32] primary plasma that acts as an initial explosion energy source and emits an intense continuum emission background for a short time just close above the surface of the target and secondary plasma, which expands with time around the primary plasma. The secondary plasma is formed by the excitation from the shock wave and by the emitting of atomic, ionic, and molecular species characterized by a low background signal.

Figure 6(a) displays the TOF profiles for the air breakdown experiments induced by CO_2 laser pulses (106 J/cm^2), of O^+ (2433.5 and 2455.5 Å), N^+ (2461.3, 2498.8, and 2522.2 Å) and C (2478.6 Å) lines as functions of the delay time. These spectral lines in the UV correspond to the spectra of Figs. 3 and 4. For O^+ and N^+ ionic and C atomic species, the maxima appear for a delay of 2.5, 3, and 4.5 μs, respectively. The emission intensity of O^+ and N^+ ionic lines decreases more rapidly than the emission intensity of the C lines. The time duration of ionic species was nearly 5 μs, while the time duration of C atomic emission was nearly 20 μs. The experimental TOF distribution $N(t)$ is essentially number density distributions. They are converted to flux distributions, dN/dt, by employing a correction factor z/t, where z means the flight distance along the plasma expansion and t is the delay time after the laser pulse incidence. It should be mentioned that the estimation of velocity distributions assumes that the emitting species are generated on the assisting metal mesh target. The velocity distributions that are derived from these TOF distributions are displayed in Fig. 6(b). At the laser fluence used in these experiments (106 J/cm^2) and z=5 mm, TOF distributions present different characteristics. Thus, the velocity distributions of ionic species O^+(2445.54 Å) and N^+(2522.23 Å) are comparatively wider [≈3.7 and ≈4 km/s (FWHM), respectively,] than the velocity distribution of carbon neutral species [≈1.2 km/s (FWHM)]. The velocity distributions of O^+, N^+, and C lines species are centered at about 2, 1.7, and 1.1 km/s, respectively.

From TOF spectra, the translational kinetic energy can be deduced [$KE=(1/2)m(z/t)^2$] by measuring the time t required to transverse the distance from the target to the detector z. The kinetic energy obtained for some species are plotted in Fig. 7. We have observed small atomic and ionic average kinetic energies. As we have stated above, for a better understanding of the physical mechanisms underlying the plasma emission breakdown in air, LIB spectra were obtained by varying both the distance z (up to 10 mm) with respect to the auxiliary metal mesh and the laser energy. It is expected, in fact, that these two parameters would affect strongly the dynamic evolution of the plasma and the shock wave induced by the CO_2 laser. Different lines, originating from atomic and ionic species of nitrogen and oxygen, were analyzed. O^+ doublet

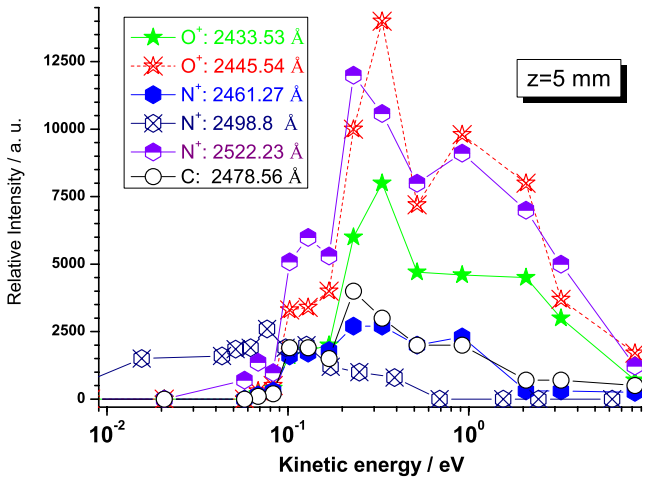

FIG. 7. (Color online) Kinetic energy distributions of the O^+(2433.53 Å), O^+(2445.54 Å), N^+(2461.27 Å), N^+(2498.8 Å), N^+(2522.23 Å), and C(2478.56 Å) lines derived from the TOF spectra at z=5 mm.

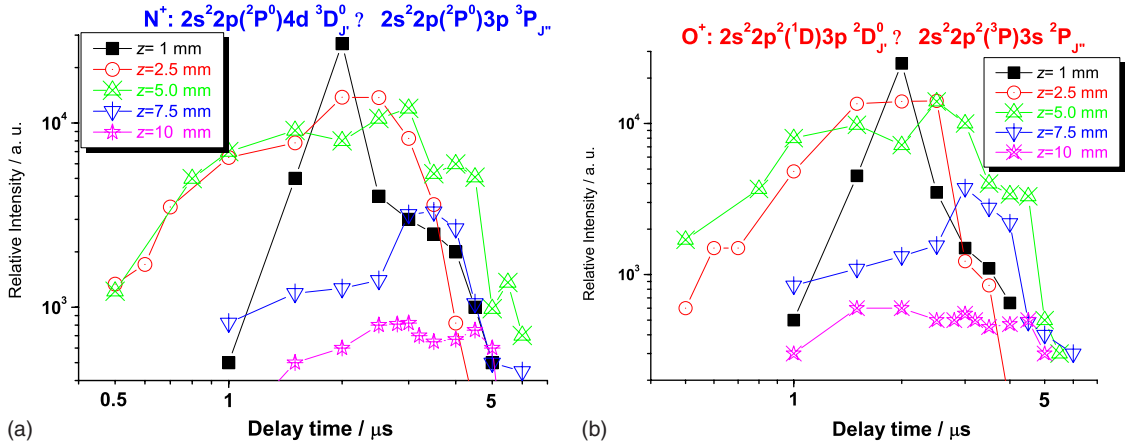

FIG. 8. (Color online) Number density TOF profiles of multiplet structures of N^+(≈2522 Å) and O^+(≈2445 Å) at 1, 2.5, 5, 7.5, and 10 mm as a function of the delay time for a laser fluence of 106 J/cm^2.

$(2s^22p^2(^1\mathrm{D})3p\ ^2\mathrm{D}^0_{3/2,5/2} \rightarrow 2s^22p^2(^3\mathrm{P})3s\ ^2\mathrm{P}_{3/2})$ at ≈2445 Å and N^+ triplet $(2s^22p(^2\mathrm{P}^0)4d\ ^3\mathrm{D}^0_{1,2,3} \rightarrow 2s^22p(^2\mathrm{P}^0)3p\ ^3\mathrm{P}_{0,1,2})$ at ≈2522 Å were chosen as a representative of ionized lines. The energies of the lower levels of both multiple are high[33] (189 068.514 for O^+ and 170 572.61, 170 607.89, and 170 666.23 cm^{-1} for N^+) so that the self-absorption effect can be neglected. Figures 8 and 9 show TOF and velocity distributions of multiplet structures of N^+(≈2522 Å) and O^+(≈2445 Å) at different distances (1, 2.5, 5, 7.5, and 10 mm). The temporal emission features are affected by the presence of the strong continuum at short distances ($z \leq 3$ mm) and at early delay times. However, at distances greater than 3 mm, the continuum radiation is considerably reduced and the interference of the continuum on the TOF distributions is negligible. The spike observed in TOF and velocity profile is the prompt signal that is used as a time maker. By the shift in the TOF peaks for each distance it is possible to approximately calculate the mean velocities of LIB along the propagation axis *Z*. The measured peak velocities of multiplet structures of N^+(≈2522 Å) and O^+(≈2445 Å), monitored at 1, 2.5, 5, 7.5, and 10 mm are 0.5, 1, 1.7, 2.1, and 3.6 km/s and 0.5, 1, 2, 2.5, and 5 km/s, respectively. The peak velocities of N^+ and O^+ increase with the distance from the target surface. This trend has been reported previously,[34] and is due to the initial acceleration of the ablated particles from zero velocity to a maximum velocity.

The different components of the velocity distributions for each species may be due to the different formation mechanism. Particularly, for A^+ species (A=N or O), the complex velocity distribution observed in Figs. 6–8 might indicate that several processes can be involved in its formation $[A+nh\nu+e^- \rightarrow A+e^{-*} \rightarrow A^++2e^-$ (inverse bremsstrahlung and electron-impact ionization); $A^{2+}+e^- \rightarrow A^+$ (electron-ion recombination) etc.]. Also, it is possible that the plasma, at some distance from the laser focal position, can be photoexcited by the strong radiation generated by the core plasma near the mesh. We have also observed that the N^+ expansion velocity has the same behavior as the O^+ expansion velocity. According to this result, the N^+ formation seems to result from the same processes than the O^+ species. On the other hand, we have studied OES of the air plasma by varying the laser energy. We have observed that when the laser fluence is increased, the N^+ and O^+ TOF distributions broaden and move toward lower delay times.

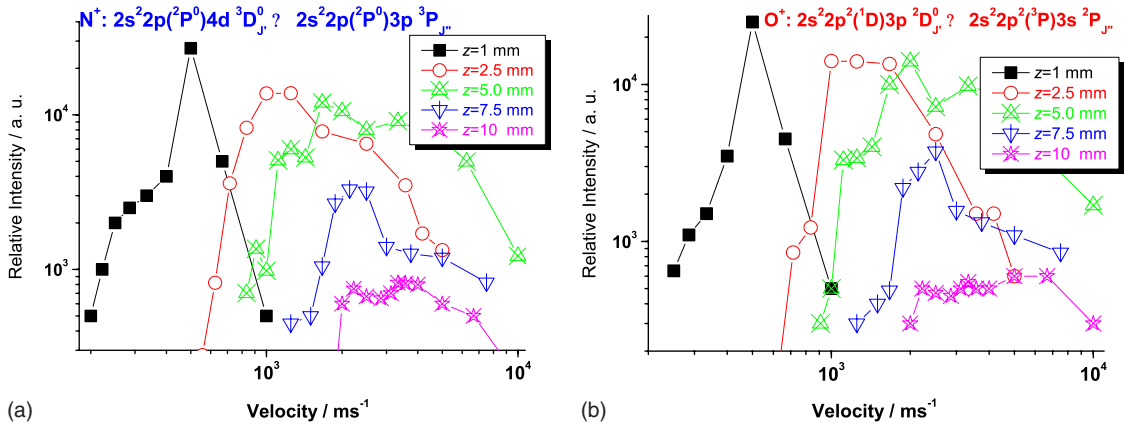

FIG. 9. (Color online) Velocity profiles of multiplet structures of N^+(≈2522 Å) and O^+(≈2445 Å) at 1, 2.5, 5, 7.5, and 10 mm as a function of delay time for a laser fluence of 106 J/cm^2.

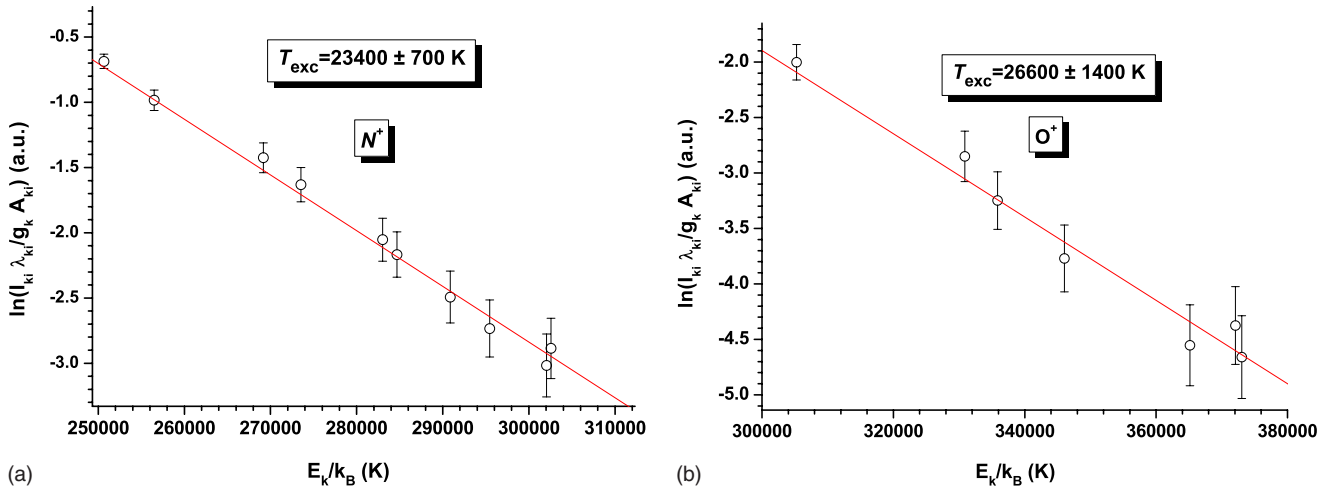

FIG. 10. (Color online) Linear Boltzmann plots for several N^+ and O^+ transition lines used to calculate plasma excitation temperature for a delay time of 3 μs. Plots also show linear fit to the data.

C. Plasma temperature and electron density

The main factors that influence the emission by the plasma are its temperature, the number density of the emitting species and the electron density. The number density of the emitting species depends on the plasma temperature, and the degree of the excitation and/or ionization of the plasma. Therefore, the knowledge of the plasma temperature and the density of the plasma species are vital for the understanding of the atomization, excitation, and ionization processes occurring in the plasma. For plasma in local thermodynamic equilibrium (LTE), the population density of atomic and ionic electronic states is described by Boltzmann distribution. The conditions satisfying this assumption of LTE require that the radiative depopulation rates to be negligible compare to the collisional depopulation rates. This essentially implies that an excited state must have a higher probability of de-excitation by collisions than by spontaneous emission. For optically thin plasma, the reabsorption effects of plasma emission are negligible. So, the emitted spectral line intensity is a measure of the population of the corresponding energy level of this element in the plasma. For LTE plasma, the temperature can be calculated from the relative intensities of several atomic or ionic lines by

$$\ln\left[\frac{I_{ki}\cdot\lambda_{ki}}{g_k\cdot A_{ki}}\right]=C-\frac{E_k}{k_B\cdot T}, \tag{1}$$

where I_{ki} is the emissivity in W m^{-3} sr^{-1} of the emitted $k\rightarrow i$ spectral line, λ_{ki} is the wavelength, $g_k=2J_k+1$ is the statistical weight, A_{ki} is the Einstein transition probability of spontaneous emission, E_k/k_B is the normalized energy of the upper electronic level, $C=\ln[hcN_k/4\pi Q(T)]$ [$Q(T)$ is the partition function] and T is the temperature. In LTE all temperatures are assumed to be equal, i.e., $T_e\approx T_{ion}\approx T_{plasma}$. The Boltzmann method implies the assumption of LTE, but given the high electron density in our plasmas (see further), this assumption seems to be satisfied at least in the initial 4 μs of the plasma lifetime. The emitted spectral line intensity from a given state of excitation can be used to evaluate the plasma temperature. By plotting the left hand side of Eq. (1) versus the excited level energy E_k, the plasma temperature can be obtained from the slope of the obtained straight line. The plasma temperature is determined from the emission line intensities of several N^+ and O^+ ionized lines observed in the laser-induced plasma of air for a delay time of 3 μs and a distance of $z=5$ mm. The spectral line wavelengths, energies of the upper levels, statistical weights, and transition probabilities used for these lines are obtained from National Institute of Standards and Technology (NIST).[33] The obtained excitation temperatures, in the case of N^+ and O^+, are 23 400 ± 900 K and 26 600 ± 1300 K, respectively. The corresponding Boltzmann plots are shown in Fig. 10. Real plasmas provide, even in the best cases, just an approximation to LTE. However, their spatial inhomogeneity is very large as concerns to the temperature and number density distributions of the different species. Consequently, the LTE occurs only within a very small volume of the plasma.

Spectral lines are always broadened, partly due to the finite resolution of the used spectrometer and partly to intrinsic physical causes. The principal physical causes of the spectral line broadening are the Doppler and Stark broadening. Stark line broadening from collisions of charged species is the primary mechanism influencing the emission spectra in these experiments. The electron number density can be obtained from the Stark broadening of the emission lines. In our experiments, for N^+ and O^+ lines, the Doppler line widths vary between 0.08–0.17 Å at 23 400 K and 0.11–0.13 Å at 26 600 K, respectively. The width of Stark broadening spectral line depends on the electron density n_e. Both the linear and the quadratic Stark effect are encountered in spectroscopy. For a non-H-like line, the electron density n_e (in cm^{-3}) could be determined from the FWHM of the line from the approximated formula[35]

$$\Delta\lambda^S_{FWHM}=2W\left(\frac{n_e}{10^{16}}\right), \tag{2}$$

where W is the electron-impact parameter (Stark broadening value). The N^+ triplet $(2s^22p(^2P^0)4d\ ^3D^0_{1,2,3}\rightarrow 2s^22p(^2P^0)3p\ ^3P_{0,1,2})$ at ≈2522 Å was identified as a can-

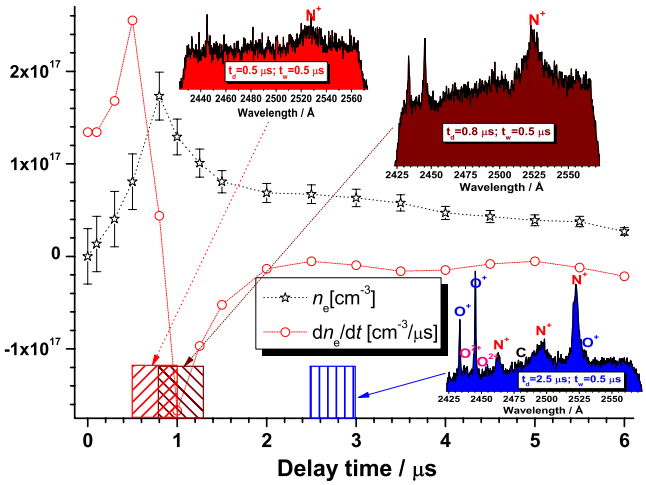

FIG. 11. (Color online) Temporal evolution of electron density n_e and dn_e/dt for different delay times from plasma ignition and $z=5$ mm. Inset plots illustrate some spectra observed at different delay times.

didate for electron-density measurements. By substituting the Stark line widths at different time delays in Eq. (2) and the corresponding value of Stark broadening W (0.372 Å from Griem[35] at plasma temperature of 23 400 K), we obtain the electron density.

D. Ionization and recombination processes

From the time evolution of electron density some consideration about ionization and recombination processes can be made. Figure 11 gives this time evolution of electron density and its first derivative with respect to time by setting the gate width of the intensifier at 0.5 μs. These values have been obtained from spectra recorded at z=5 mm and for a laser fluence of 106 J/cm^2. The initial electron density at 0.1 μs is approximately 1.3×10^{16} cm^{-3}. Afterwards, the density increases and reaches a maximum (1.7×10^{17} cm^{-3}) at $\approx$0.8 μs, and then decreases as the time is further increased. At shorter delay times ($<$0.1 μs), the line to the continuum ratio is small and the density measurement is sensitive to errors in setting the true continuum level. For times $>$0.1 μs, the line to the continuum ratio is within the reasonable limits and the values of electron density shown in Fig. 11 should be reliable. After 6 μs, the electron density is about 2.7×10^{16} cm^{-3}. For a long time $>$6 μs, subsequent decreased N$^+$ emission intensities result in poor signal-to-noise ratios, and there is a limitation in the spectral resolution. The decrease in n_e is mainly due to recombination between electrons and ions in the plasma. These processes correspond to the so-called radiative recombination and three-body recombination processes in which a third body may be either a heavy particle or an electron. The electron number density n_e (cm^{-3}) in the laser-induced plasma is governed by the kinetic balance equation[35,36]

$$\frac{dn_e}{dt} = k_{ion} n_e N_i - k_{rec} n_e^3, \tag{3}$$

where N_i indicates the concentration of heavy particles (cm^{-3}) and k_{ion} (cm^3 s^{-1}) and k_{rec} (cm^6 s^{-1}) denote the rate constants of ionization ($e^- + A \rightarrow A^+ + 2e^-$) and three-body electron-ion recombination ($2e^- + A^+ \rightarrow A^* + e^-$), respectively. Equation (3) is an approximation of a most general equation that includes several terms corresponding to another loss and formation mechanisms (diffusion loss, electron attachment, etc.). In our experimental conditions, these terms are negligible. In particular, the term due to diffusion loss depends on the focal volume and has a Λ^{-2} dependence, being Λ the diffusion length. In our case $\Lambda \approx 21\times10^{-3}$ cm,[23] therefore, we have a large focal volume. The excess of energy in three-body electron-ion recombination goes to kinetic energy of a free electron, which participates in the recombination act as a third body partner. It should be noted that heavy particles (neutrals and ions) are unable to accumulate electron recombination energy fast enough in their kinetic energy and are ineffective as the third body partner. The three-body electron-ion recombination energy can be converted into radiation in the process of radiative electron-ion recombination ($e^- + A^+ \rightarrow A^* \rightarrow A + h\nu$). The cross section of this process is relatively low, and it can be competitive with three-body electron-ion recombination only when the plasma density is low. If $dn_e/dt=0$ an equilibrium condition can be established; if $dn_e/dt \neq 0$, then the ionization ($dn_e/dt>0$) or three-body recombination ($dn_e/dt<0$) prevails and the departure from the equilibrium occurs.[36] From Fig. 11 the equilibrium condition can be established at 0.8 μs (dynamical equilibrium) and $t>2$ μs (stationary equilibrium). For $t \leq 0.8$ μs the ionization prevails while for 0.8 $\mu s < t < 2$ μs the three-body recombination dominates. The second derivative of $Y=dn_e/dt$ with respect to the electron number density is given by

$$\frac{d^2Y}{dn_e^2} = -6k_{rec}n_e. \tag{4}$$

In the case of the TEA-CO$_2$ laser, at a laser fluence of 106 J/cm^2 and $z=5$ mm, the estimated recombination rate constant is approximately 5×10^{-28} cm^6 s^{-1}. The recombination time can be determined by the value of the rate constant of the recombination process as $t_{rec}=1/(n_e^2 k_{rec})$,[36,37] obtaining $t_{rec} \approx 0.4-3$ μs.

Optical emission accompanying TEA CO$_2$ nanosecond LIB in the air is very long lived ($\approx$20 μs) relative to the average radiative lifetimes of the excited levels that give rise to the observed emission lines. All the emission lines of N, N$^+$, N^{2+}, O, O$^+$, and O^{2+} expected in the 2000–10 000 Å wavelength range are observed,[33] illustrating that the excited species giving rise to the optical emission are produced by a nonspecific mechanism during the TEA CO$_2$ LIB process. However, a direct excitation-de-excitation mechanism cannot explain the observed emission spectra. Electron impact ionization would explain the emission intensity variation with the time for N, N$^+$, N^{2+}, O, O$^+$, and O^{2+} species. On the other hand, the formation of the excited molecular species would happen in the gas phase by collisions between atomic or ionic species present in the plasma at times far away from the plasma ignition. The emission process at this plasma stage is divided into two different process associated, respectively, with the shock formation and the plasma cooling. During the former, the atoms, molecules and ions gushing out from the laser focal region are adiabatically compressed

against the surrounding gas. In the latter stage, the temperature of the plasma and consequently the emission intensities of atomic, ionic lines and molecular bands, decrease gradually.

IV. CONCLUSION

The high density air plasma generated by CO_2 laser pulses at $\lambda = 10.591$ μm has been investigated spatially and temporally by spectroscopic measurements. The study has been carried out in a regime of relatively high laser fluences ($70-160$ J/cm^2). The emissions observed are due to electronic relaxation of excited N, O, C, H, Ar, and ionic fragment N^+, O^+, N^{2+}, O^{2+}, C^+, and molecular band systems of $N_2^+(B\ ^2\Sigma_u^+ - X\ ^2\Sigma_g^+)$, $N_2(C\ ^3\Pi_u - B\ ^3\Pi_g)$, $N_2^+(D\ ^2\Pi_g - A\ ^2\Pi_u)$, and $OH(A\ ^2\Sigma^+ - X\ ^2\Pi)$. The characteristics of the spectral emission intensities for some species have been investigated as a function of the delay time after plasma formation. The initial plasma ($0.1\ \mu s < t_d < 2\ \mu s$), near the focal region ($z < 2.5$ mm), is characterized by high continuum background and high electron and ion densities $[(0.13-1.7) \times 10^{17}\ \text{cm}^{-3}]$. The velocity and kinetic energy distributions for different species were obtained from TOF measurements using time resolved OES. The temperature measurements have been performed by Boltzmann diagram method using N^+ and O^+ lines. Electron density estimations were made by using Stark broadening method. Time-resolved studies of electron density and temperatures have been carried out using emission lines of N^+. Temporal evolution of electron number density has been used for the estimation of the three-body recombination rate constant.

ACKNOWLEDGMENTS

We gratefully acknowledge the support received in part by the DGICYT (Spain) Projects: MEC: CTQ2007-60177/BQU and MEC: CTQ2008-05393/BQU for this research.

[1] P. D. Maker, R. W. Terhune, and C. M. Savage, *Proceedings of the Third International Conference Quantum Electronics* (Dunod, Paris, 1963), Vol. 2, p. 1559.
[2] Y. P. Raĭzer, Sov. Phys. Usp. **8**, 650 (1966).
[3] Y. P. Raizer, *Laser-Induced discharge phenomena* (Consultants Bureau, New York, 1977).
[4] C. DeMichelis, IEEE J. Quantum Electron. **5**, 188 (1969).
[5] C. G. Morgan, Rep. Prog. Phys. **38**, 621 (1975).
[6] G. Bekefi, *Principles of Laser Plasma* (Wiley, New York, 1976).
[7] J. L. Lyman, G. P. Quigley, and O. P. Judd, in *Multiple-Photon Excitation and Dissociation of Polyatomic Molecules*, edited by C. D. Cantrell (Springer, New York, 1980).
[8] D. I. Rosen and G. Weyl, J. Phys. D **20**, 1264 (1987).
[9] Y. E. E.-D. Gamal, J. Phys. D **21**, 1117 (1988).
[10] D. C. Smith, Laser induced gas breakdown and plasma interaction 38th Aerospace Sciences Meeting and Exhibit, Reno, American Institute of Aeronautics and Astronautics, Paper No. 2000-0716, 2000
[11] M. S. Tillack, D. W. Blair, and S. S. Harilal, Nanotechnology **15**, 390 (2004).
[12] D. A. Cremers and L. J. Radziemski, *Handbook of Laser-Induced Breakdown Spectroscopy* (Wiley, New York, 2006).
[13] A. W. Miziolek, V. Palleschi, and I. Schechter, *Laser-Induced Breakdown Spectroscopy* (Cambridge University Press, Cambridge, 2006).
[14] J. P. Singh and S. N. Thakur, *Laser-Induced Breakdown Spectroscopy* (Elsevier, New York, 2007).
[15] A. M. Marpaung, H. Kurniawan, M. O. Tjia, and K. Kagawa, J. Phys. D **34**, 758 (2001).
[16] C. V. Bindhu, S. S. Harilal, M. S. Tillack, F. Najmabadi, and A. C. Gaeris, Appl. Spectrosc. **58**, 719 (2004).
[17] V. Hohreiter, J. E. Carranza, and D. W. Hahn, Spectrochim. Acta, Part B **59**, 327 (2004).
[18] N. Glumac and G. Elliott, Opt. Lasers Eng. **45**, 27 (2007).
[19] N. Kawahara, J. L. Beduneau, T. Nacayama, E. Tomita, and Y. Ikeda, Appl. Phys. B: Lasers Opt. **86**, 605 (2007).
[20] P. K. Diwakar and D. W. Hahan, Spectrochim. Acta, Part B **63**, 1038 (2008).
[21] J. J. Camacho, J. M. L. Poyato, L. Diaz, and M. Santos, J. Phys. B **40**, 4573 (2007).
[22] J. J. Camacho, M. Santos, L. Diaz, and J. M. L. Poyato, J. Phys. D **41**, 215206 (2008).
[23] J. J. Camacho, L. Diaz, M. Santos, L. J. Juan and J. M. L. Poyato, Appl. Phys. A **99**, 159 (2010).
[24] J. J. Camacho, L. Diaz, M. Santos, L. J. Juan, and J. M. L. Poyato, J. Appl. Phys. **106**, 033306 (2009).
[25] A. De Giacomo, Spectrochim. Acta, Part B **58**, 71 (2003).
[26] M. Rossa, C. A. Rinaldi, and J. C. Ferrero, J. Appl. Phys. **105**, 063306 (2009).
[27] A. I. Barchukov, F. V. Bunkin, V. I. Konov, and A. A. Lyubin, Sov. Phys. JETP **39**, 469 (1974).
[28] S. Marcus, J. E. Lowder, and D. L. Mooney, J. Appl. Phys. **47**, 2966 (1976).
[29] J. F. Ready, *Effect of High Power Laser Radiation* (Academic, New York, 1971).
[30] J. M. Vadillo, F. Romero, C. Rodrigues, and J. J. Laserna, Surf. Interface Anal. **27**, 1009 (1999).
[31] P. De Montgolfier, P. Dumont, Y. Mille, and J. Villermaux, J. Phys. Chem. **76**, 31 (1972).
[32] K. Kagawa and S. Yokoi, Spectrochim. Acta, Part B **37**, 789 (1982).
[33] NIST Atomic Spectra Database online at http://physics.nist.gov/PhysRefData/ASD/index.html.
[34] S. S. Harilal, B. O'Shay, and M. S. Tillack, J. Appl. Phys. **98**, 013306 (2005).
[35] H. R. Griem, *Principles of Plasma Spectroscopy* (Cambridge University Press, Cambridge, 1997).
[36] M. Capitelli, F. Capitelli, and A. Eletskii, Spectrochim. Acta, Part B **55**, 559 (2000).
[37] M. Capitelli, A. Casavola, G. Colonna, and A. D. Giacomo, Spectrochim. Acta, Part B **59**, 271 (2004).